Evolution of Collective, Radiative Plasmon Coupling in Confined, Soft Colloidal Films

Déborah Feller, Jiakai Wang, Julian Kippenberger, Christian Washeim, Jan A. Meissner, Jan Meisner, Paul Mulvaney, Matthias Karg

RESEARCH ARTICLE

ADVANCED OPTICAL MATERIALS
www.advopticalmat.de

Evolution of Collective, Radiative Plasmon Coupling in Confined, Soft Colloidal Films

*Déborah Feller, Jiakai Wang, Julian Kippenberger, Christian Washeim, Jan A. Meissner, Jan Meisner, Paul Mulvaney, and Matthias Karg**

Plasmon resonance coupling is a strongly distance-dependent phenomenon that also critically depends on the spatial arrangement of its plasmonic constituents, for example, plasmonic nanoparticles in periodic or random assemblies. Here, we report electromagnetic coupling in ordered monolayers of gold nanoparticles. The interparticle distances range from two to almost six times the particle diameter. This is achieved by continuously monitoring the optical response of a soft colloidal monolayer film that is confined at the air/water interface and compressed through the barriers of a Langmuir trough. The colloidal building blocks contain monodisperse, spherical gold nanoparticles that are homogeneously encapsulated in soft, deformable microgel shells. The soft shell enables continuous tuning of the interparticle distance. This work directly compares the optical response measured in situ at the fluid interface to the response of monolayers that are transferred to glass substrates. Supported by COMSOL simulations and calculations using the coupled dipole approximation this work observes plasmonic surface lattice resonances for large spacings at the fluid interface. Reducing the interparticle distance leads to increased damping and broadening of the coupled resonances. These results demonstrate the feasibility of engineering 2D plasmonic structures with a wide range of optical properties via mechanical manipulation of soft colloidal films.

1. Introduction

Nanocrystals (NCs) can be synthesized with excellent control over their size, shape and their polydispersity – parameters that define the optical, electrical and magnetic properties of these nanoscale building blocks.[1–5] When NCs are assembled into ordered 2-D or 3-D superstructures new nanomaterials with unique properties can be tailored.[6–9] Crucial for structural control are the surface properties that ultimately define the colloidal interactions.

Common examples are steric stabilizers such as macromolecular ligands[10–15] or polymeric networks that encapsulate the NCs.[16–19] Depending on the molecular weight of such surface decorations, different regimes of interparticle spacing can be entered: Macromolecular ligands typically cover interparticle distances ranging from ≈0.1 to 10 nanometers while cross-linked polymer shells such as hydrogel shells, cover spacings from tens to many hundreds of nanometers depending on the shell thickness.[20]

Such polymeric coatings not only render NCs colloidally stable but endow them with long-range soft interactions.[21–23] In contrast to rigid bodies with a steep interaction potential, soft colloidal building blocks can be assembled into periodic superstructures with a range of periodicities that are governed by the packing fraction.[24–27] For example, when confined at a fluid interface, that is, air/water or oil/water interfaces, reduction of the available interfacial area leads to a compression of the thin colloidal film with a continuous decrease in interparticle spacing.[28–30] When using core-shell (CS) building blocks with NC cores and thick CS microgels, materials with the same lattice structure but with varying lattice constants can be fabricated using one type of building block.[31–36] This is particularly interesting for studying distance-dependent

D. Feller, J. Kippenberger, C. Washeim, M. Karg
Institut für Physikalische Chemie I: Kolloide und Nanooptik
Heinrich-Heine-Universität Düsseldorf
Universitätsstr. 1, 40225 Düsseldorf, Germany
E-mail: matthias.karg@chemie.uni-halle.de

The ORCID identification number(s) for the author(s) of this article can be found under https://doi.org/10.1002/adom.202501657

DOI: 10.1002/adom.202501657

J. Wang, P. Mulvaney
ARC Centre of Excellence in Exciton Science
School of Chemistry
The University of Melbourne
Parkville, VIC 3010, Australia

J. A. Meissner, J. Meisner
Institut für Physikalische Chemie
Heinrich-Heine-Universität Düsseldorf
Universitätsstr. 1, 40225 Düsseldorf, Germany

M. Karg
Physical Chemistry of Functional Polymers
Institute of Chemistry
Martin Luther University Halle-Wittenberg
06120 Halle (Saale), Germany

collective effects. One important example of this is the electromagnetic coupling between plasmonic NCs. At small interparticle distances localized surface plasmon resonances (LSPR) couple via the electric near field.[9,37–39] At distances that are significantly larger than the individual NC diameter, long-range radiative coupling via the far field can be observed. In 2D periodic arrays of NCs with wavelength-scale interparticle distances (divided by the local refractive index)[40] such radiative coupling can lead to collective interference modes. The resulting narrow linewidths resonances are known as plasmonic surface lattice resonances (SLRs) or lattice plasmons (LPs).[33,41–43] Understanding, tuning and optimizing such coupling effects has been an intense field of research for the last decade.[40,41,44,45] However, most of the studies so far rely on investigation of superstructures on solid supports and the one-to-one preparation and investigation of samples. A few studies exist where flexible substrates were used to post-modify the lattice spacing and/or lattice geometry via substrate deformation.[46–48] However, approaches that can maintain the lattice structure while allowing dynamic control over the lattice period have not been demonstrated to date.

In this work, we present a method to directly modulate the optical response of assembled plasmonic CS microgels at the air/water interface in situ in a Langmuir trough using uniaxial compression. We are able to monitor in real-time the optical behavior and to record spectra at 1-s intervals, resulting in more than 1800 spectra for one compression cycle of the colloidal film. Our in situ spectroscopic measurements allow us to relate resonance position, strength and width to changes in interparticle distance from almost six down to two times the core diameter. The optical response of the colloidal film can be recorded as a function of the interparticle distance for step-sizes down to 0.2 nm. We observe a continuous blueshift and broadening of the resonance peak with decreasing interparticle distance. Our findings are directly compared to spectral results from colloidal films transferred to solid (glass) substrates. COMSOL simulations and calculations using coupled dipole approximation were also performed to interpret the experimental trends. The results demonstrate the feasibility of creating large-scale, tunable plasmonic structures via simple mechanical manipulation of self-assembled films of colloidal building blocks. This new spectroscopic approach also provides insights into the phase behavior of soft colloidal monolayers confined at fluid interfaces.

2. Experimental section

2.1. Materials

Gold(III) chloride trihydrate ($HAuCl_4 \cdot 3H_2O$; Sigma-Aldrich, ≥ 99.999%), sodium citrate dihydrate (Sigma-Aldrich, ≥ 99%), sodium dodecyl sulfate (SDS; Sigma-Aldrich, p.a.), butenylamine hydrochloride (BA; Sigma-Aldrich, 97%), *N*,*N*′-methylenebisacrylamide (BIS; Sigma-Aldrich, ≥ 99%), potassium peroxodisulfate (PPS; Sigma-Aldrich, ≥ 99%), cetyltrimethylammonium chloride (CTAC; Sigma-Aldrich, 25 wt% in water), ascorbic acid (Roth, p.a.), 1H,1H,2H,2H-Perfluorooctyltriethoxysilane (FOCTS; J&K Scientific, 97%), ethanol (Honeywell, p. a.), ammonia (PanReac Applichem, 30% in water), hydrogen peroxide (Fisher Scientific, > 30% in water), cyclohexane (Fisher Scientific, ≥ 99.8%), and Hellmanex III (Hellma GmbH) were used as received. *N*-isopropylacrylamide (NIPAM; TCI, > 98.0%) was recrystallized from cyclohexane. Milli-Q water (Millipore, resistivity > 18 MΩcm) was used for all syntheses and Langmuir trough experiments.

2.2. Synthesis

2.2.1. Synthesis of Core-Shell Microgels

Monodisperse, nanocrystalline gold nanoparticles (AuNPs) of near spherical shape were synthesized using the established Turkevich method.[49] This yielded AuNPs with a diameter of 14.1 ± 1.1 nm determined by TEM analysis of at least 150 particles. These NPs were then used as seeds in a seeded precipitation polymerization to synthesize Au-PNIPAM CS microgels following the protocol reported by Rauh et al.[50] In short, the surface of the AuNP seeds was functionalized with BA prior to the encapsulation. NIPAM as monomer and BIS as chemical crosslinker (16.7 mol % (nominal) with respect to the amount of NIPAM) were used to grow the microgel shell. PPS was used as radical initiator. Upon successful encapsulation and purification, the CS microgels were used to overgrow the AuNP cores to enhance the plasmonic properties. The overgrowth of the cores was done following a protocol reported previously (Ponomareva et al.).[33] After multiple steps of overgrowth, the AuNP cores reached a size of 96.3 ± 8.2 nm in diameter. The details of the synthesis can be found in the **Supporting Information**. The CS structure of the microgels with the hydrodynamic diameter D_h is schematically shown in **Figure 1a**. A TEM image of the final CS microgels is shown in Figure 1d.

2.2.2. Preparation of Glass Substrates for Monolayer Transfer

Standard microscopy slides were cleaned by the RCA-1 method.[51] This involved mixing five parts of water with one part of ammonia solution (30%) and heating the mixture to 80 °C under stirring. Once this temperature was reached, one part of H_2O_2 solution (30%) was added. The glass slides were then immersed in the solution for 15 min and the solution temperature was maintained between 75 and 85 °C. Afterward, the glass slides were removed and thoroughly rinsed with water. Before drying with a stream of compressed N_2, the cleaned substrates were left in water for an additional 5 min. The hydrophobization of the glass slides was carried out using chemical vapor deposition. The slides were placed in a desiccator with 120 µL FOCTS and the pressure was reduced to 150 mbar. The functionalization was allowed to proceed overnight. Following this, the glass slides were removed and treated at 60 °C in an oven for 2 h. Afterward, the slides were sonicated for 10 min in ethanol and then dried with N_2. The slides were cut in half along the length and horizontal lines were scratched on the back of the slide for further use. From the bottom of the slide, five lines with a distance of 1 cm and a last line with a distance of 0.5 cm were marked.

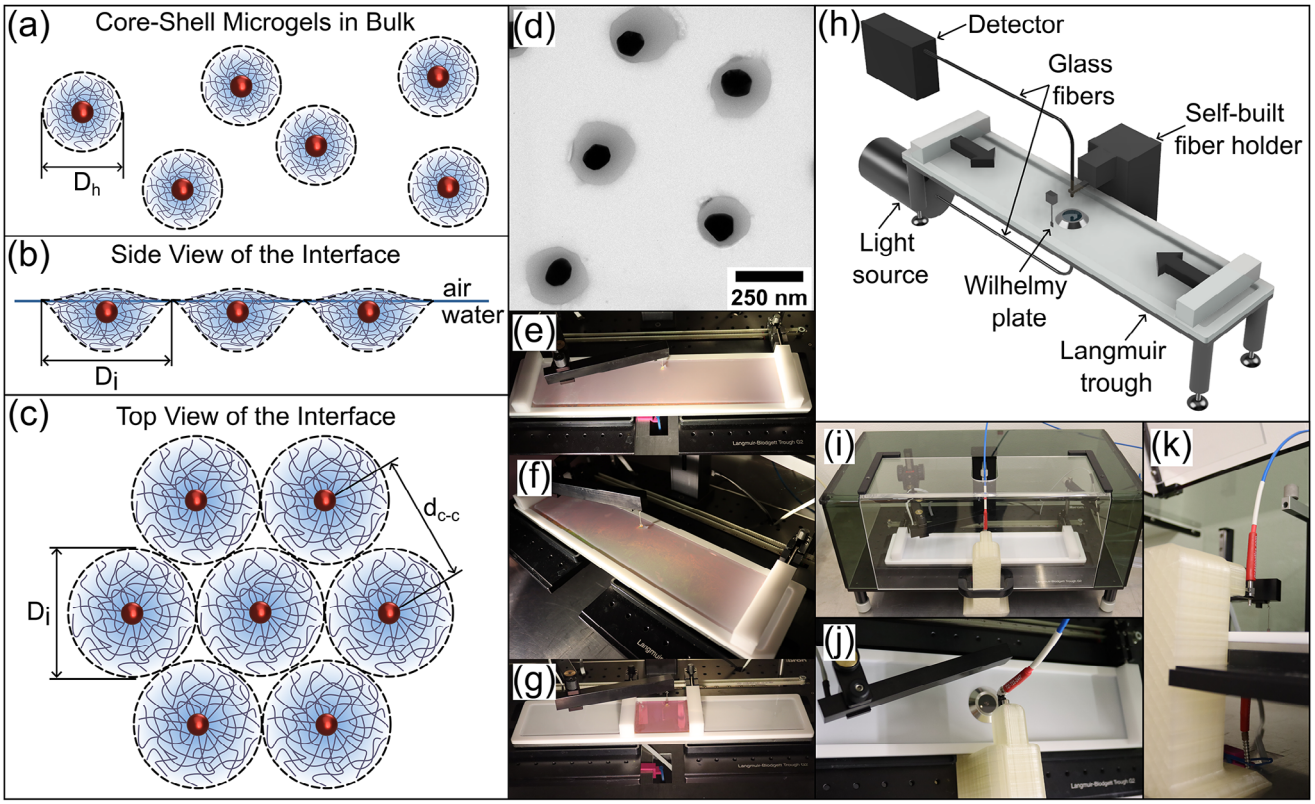

Figure 1. a) Illustration of the structure of the CS microgels in bulk with the hydrodynamic diameter D_h indicated as dashed circles. b) Side and c) top view of the microgels hexagonally assembled at the air/water interface with the diameter at the interface D_i highlighted by the dashed circles. d) Representative TEM image of the microgels. Photographs of the microgels assembled at the air/water interface at e,f) low and g) high compression. h) 3D illustration of the setup combining extinction spectroscopy with a Langmuir trough. The large arrows show the direction of the movement of the barriers. i–k) Photographs of the experimental set up with the self-built fiber holder with mounted optical fibers taken from different perspectives.

3. Methods

3.1. Atomic Force Microscopy

AFM height images were recorded in intermittent contact mode in air using a Nanowizard 4 (JPK Instruments). Imaging was performed with OTESPA-R3 AFM probes (Bruker), that feature a visible apex tip geometry with a nominal tip radius of 7 nm. The cantilevers had a resonance frequency of 300 kHz and a spring constant of 26 N m^{-1} according to the manufacturer. Exact values were not measured. The images were tilt-corrected and flattened with the JPK Data Processing software and further analyzed with the software ImageJ.[52]

3.2. Transmission Electron Microscopy

TEM imaging was performed with a JEOL JEM-2100Plus TEM in bright-field mode using an acceleration voltage of 80 kV. The samples were prepared on carbon-coated copper grids (200 mesh, Electron Microscopy Science) by drop-casting 7 µL of a dilute aqueous microgel dispersion. The grids were dried at room temperature. Core sizes were measured using the software ImageJ.[52]

3.3. Dynamic Light Scattering

DLS measurements were carried out with a Zetasizer Nano S (Malvern Panalytical). The laser had a wavelength of 633 nm and the scattered light was detected at a scattering angle of 173 °. A dilute aqueous CS microgel dispersion was measured three times for 60 s in a semi-macro cuvette (polymethacrylate, VWR). The hydrodynamic diameter, D_h, (z-average) was determined by cumulant analysis via the instrument software.

3.4. Extinction Spectroscopy

Extinction spectra were recorded using a Specord S 600 UV–vis spectrophotometer (Analytik Jena AG) over a wavelength range of 250 – 1019 nm. The spectra of dilute samples were measured in transmission geometry using PMMA cuvettes with 1 cm pathlength. Water was measured as background. Substrate supported monolayer samples (on glass) were placed vertically in the light path with the monolayer facing the detector. We recorded spectra at each marked line. Clean glass slides were measured as background.

3.5. Computational Simulation

A finite element analysis (FEA) method was used to simulate the near-field electric field distribution and optical extinction of the hexagonally close-packed (HCP) AuNPs with COMSOL Multiphysics Wave Optics Module. The simulation solves Maxwell's equations in the frequency domain to model the interaction of electromagnetic waves (EM waves) with the AuNP monolayer, governed by the Equation 1.

$$\nabla \times \frac{1}{\mu_r} (\nabla \times E) - k_0^2 \left(\in_r - \frac{j\sigma}{\omega \in_0} \right) E = 0 \quad (1)$$

where E is the electric field, $\nabla \times E$ is the curl of the electric field, μ_r is the relative permeability, k_0 is the free-space wavenumber, $\in_r$ is the relative permittivity, σ is the conductivity of the material, ω is the angular frequency of the wave and $\in_0$ is the vacuum permittivity. Electromagnetic differential equations are solved to model wave propagation and interactions within the system.

The model consists of two parts: the physical domain and the perfectly matched layers (PMLs). The physical domain consists of two layers: an air layer and an environment layer containing the HCP AuNPs. The HCP unit cell comprises of a whole AuNP with a radius of 46 nm placed in the center and four quarter-spheres at the corners. The environment layer has the same thickness as the diameter of the AuNPs, and the air layer is directly above the environment layer. Periodic boundary conditions are applied along both the x- and y-axes to simulate an infinite monolayer array. Perfectly matched layers (PMLs) are set to surround the entire physical domain to absorb any outgoing waves and prevent internal reflections which may interfere with the simulations. A periodic port was set at the boundary between the environment layer and the bottom PML for excitation of the incident wave. A second periodic port was set at the boundary between the air layer and the top PML for the measurement of transmittance. The incident wave was set to be normal to the AuNP monolayer, x-polarized, with an electric field amplitude of 1 V m^{-1} and an input power of 1 W. The refractive index of air was set to be 1.0, and the optical constants of gold (n and k) were sourced from Babar and Weaver.[53] Different illustrations of the simulation environments are depicted in Figures S1–S3, Supporting Information.

3.6. Compression Experiments

For compression experiments, we used polytetrafluorethylene (PTFE) barriers and a film balance to measure the surface pressure (π). Prior to the experiment, the trough and the barriers were rigorously cleaned with water, followed by ethanol and water. Before installing the Wilhelmy plate to the film balance, it was heated in a flame until red-hot to remove any residues. The clean trough was filled with water while the barriers were closed until the water reached the edges of the trough. Then the barriers were opened and the Wilhelmy plate was immersed in the water at the middle of the trough, but in the last third of the width of the trough. The microgels were applied only if π was below 0.1 mN m^{-1}. For our experiments, we applied 70 µL of the diluted stock solution at the air/water interface using a micropipette. The side view of the microgels at the interface with their interfacial diameter D_i is schematically shown in Figure 1b. The microgels are expected to show a ´fried-egg´ like shape at the interface with D_i larger than D_h.[25,54] As schematically shown in the top view of the interface in Figure 1c, the microgels arrange into a hexagonally ordered assembly with the spacing here denoted as nearest neighbor center-to-center distance $d_{c\text{-}c}$.[25,55,56] In Figure 1e,f, photographs of the interface with open barriers are depicted. The light pinkish color is attributed to the surface plasmon resonance of the AuNP cores that are part of the immersed colloidal film. In addition, the slightly visible iridescence provides evidence for the periodic arrangement of the CS microgels in the thin colloidal film. After 15 min equilibration time, we started to close the barriers at a speed of 10 mm min^{-1}. A photograph with fully closed barriers is depicted in Figure 1g. Here the intense pink color indicates that the distance between the AuNPs is reduced compared to the start. Thus, compressed microgels are assembled at the interface.

3.7. Continuous Monolayer Transfer for Ex Situ Analysis

To analyze the microstructure of the CS microgels assemblies, we performed Langmuir-Blodgett (LB) deposition onto a glass substrate that was continuously retracted through the air/water interface during reduction of the surface area.[25,28,55,57] We used the LB trough (Microtrough G2, Kibron Inc.) and a dip-coater to retract the glass slide. The glass slide was mounted on the dip coater at the center of the trough. The glass slide was placed perpendicular to the air/water interface and parallel to the barriers and then immersed at a depth of 55 mm below the interface, so that the meniscus of the water level touched the upper mark. The glass slide was retracted as soon as the compression started. The retraction speed of the dip coater (1.719 mm min^{-1}) was adjusted to the closing speed of the barriers. Thus, it was possible to map spatial positions on the substrate after the experiment to the surface pressure at the interface during the experiment. After complete drying of the glass slide, AFM height images were recorded at the marked positions. The nearest neighbor center-to-center distance ($d_{c\text{-}c}$) was determined from the radial distribution function (RDF).

3.8. In Situ Spectroscopic Investigation During Uniaxial Monolayer Compression

For the in situ experiments, we used a microscopy trough (Microtrough G2, Kibron Inc.) which was combined with a fiber-optic-based VIS-NIR spectrometer (Ocean Optics). To position the optical fibers below and above the microscopy window of the trough, we used a self-designed, 3D-printed holder. The STL file of the holder is available from the **Supporting Information**. The fiber from the light source was placed below the microscopy window of the trough (but not in contact), while the fiber leading to the detector was placed 2.6 cm above the window. The total distance between the two fibers was ≈4.4 cm. The setup is schematically shown in Figure 1h. The large black arrows indicate the direction of the compression and also that of the movement of the barriers. Photographs of the complete setup (without sample) are shown in Figure 1i–k. For better visualization, the cover box was removed in Figure 1j,k. A tungsten halogen lamp

(HL-2000-LL, Ocean Optics) was used as light source covering a wavelength range of 360 to 2000 nm. The stability and the drift of the lamp are 0.5% and < 0.3% per hour, respectively. The lamp exhibits a bulb color temperature of 2800 K. The optical fiber (P400-1-VIS-NIR, Ocean Optics) exhibited the best efficiency over the wavelength range from 400 to 2100 nm and had a fiber core diameter of 400 ± 8 µm. As detector, we used a Sony CCD array detector (FLAME-S-VIS-NIR-ES, Ocean Optics) with 2048 pixels and a minimum integration time of 1 ms. The operating wavelength range was from 350 to 1000 nm with an optical resolution of 1.33 nm. The connected optical fiber (P600-1-VIS-NIR, Ocean Optics) exhibited the best efficiency from 400 to 2100 nm and had a fiber core diameter of 600 ± 10 µm. We used Ocean View (Ocean Optics) as software to visualize and record the spectra.

The light source was left to equilibrate for 15 min before we adjusted the integration time to ≈85% of the measured capacity of the detector. The exact integration times for all experiments are listed in Table S1, Supporting Information. Each spectrum is an average of five scans with boxcar widths of three. Reference spectra of the clean and empty air/water interface with and without illumination of the light source were recorded, respectively. For these two measurements, the ceiling light of the laboratory was switched off to eliminate any perturbation from other light sources. Extinction spectra were already recorded during the equilibration time with a time resolution of 1 s. During the following compression of the colloidal film, we recorded extinction spectra in intervals of 1 s while the surface pressure was continuously measured, leading to a total of 1856 spectra per compression. The spectra were analyzed by a self-written python script called PeakAnalyzer.

3.9. Spectroscopic Investigation of Monolayers Transferred to a Glass Substrate

The coated glass substrate was measured with the same fiber-optic based spectrometer as described in the previous section. A clean glass substrate was used to record reference spectra. Then the coated substrate was mounted into a dip-coater that allowed for continuous translational movement of the substrate between the two fibers with a speed of 1.719 mm min^{-1} starting at the first marked position. Here the coated side faced toward the detection fiber. A spectrum was recorded every second from the first marked position to the edge of the coated substrate. The first 18 spectra had to be rejected, as the fiber illuminated both the coated and uncoated areas of the substrate. Hence, the spectra were not fully representative of the monolayer on the substrate. In total, we collected 1837 spectra covering the optical response of the retracted monolayer. The recorded spectra were analyzed by a self-written python script called PeakAnalyzer.

3.10. PeakAnalyzer Script

PeakAnalyzer is an open-source Python pipeline designed to automate the extraction of peak parameters from large collections of wavelength–intensity spectra. Using a companion Jupyter notebook, raw tab-delimited files are imported into Pandas, organized into project folders, and prefiltered over a user-defined spectral range. For each spectrum, the wavelength of maximum intensity is located and a Lorentzian function with a constant offset is fitted by nonlinear least squares, yielding the peak center, amplitude, half-width at half maximum and fit quality. Optionally, raw peak and baseline values are averaged over neighboring data points for direct comparison. PeakAnalyzer then renders high-resolution plots of every data-fit overlay, compiles all metrics into a single CSV summary, and can assemble the figures into a video for dynamic inspection. The package leverages numpy, pandas, matplotlib, and scipy[58–61] and is available at GitHub: https://github.com/jthemmaster/PeakAnalyzer.

4. Results and Discussion

4.1. Monolayer Assembly and Transfer to Solid Substrate

The CS microgels were self-assembled at the air/water interface in a Langmuir trough starting with open barriers, and a maximum available surface area, A_0. The spontaneously formed colloidal film was visible by its light pinkish color as seen in **Figure 1e** that covers the whole available interface. From previous works, we know that "classical" and CS microgels assemble into single monolayers at the air/water interface.[28,62] Thus, the coloration seen in Figure 1e results from a microgel monolayer. During the following uniaxial compression, the monolayer was continuously transferred to a hydrophobically modified glass slide similar to the approach reported previously.[25] Previous works found that microgels exhibit better adhesion toward hydrophobic than hydrophilic substrates, as the polymer chains of the microgels can replace unfavorable contacts between water molecules and the hydrophobic substrate.[63] On the substrate the microgels stretch into a ´fried-egg´ like conformation to maximize the contact with the substrate, similar to the situation at the air/water interface, as schematically shown in Figure 1b.[25,54] The better adhesion to the substrate can help to counteract attractive capillary forces that alter the microgel arrangement during drying.[64] As we will see later in this work, over a certain range of $d_{c\text{-}c}$ values, capillary interactions nevertheless become relevant. Using the known speed of substrate withdrawal and the barrier speed of the LB trough, we can link the recorded surface pressure to the vertical position on the substrate. A photograph of the glass slide with the continuously transferred monolayer in **Figure 2 bottom left** reveals a color change from light pinkish at the top to intense pink at the bottom. This change is mostly attributed to an increase of the number of CS microgels per unit area. Due to the monolayer compression in the trough, that is, reduction of the available surface area, A_{trough}, $d_{c\text{-}c}$ decreases from top to bottom, that is with increasing surface pressure. Furthermore, opalescence can be observed toward the top of the substrate, corresponding to low compressions, which points to the periodic arrangement of the microgels with rather large domain sizes. The horizontal, dashed lines with the corresponding surface pressures indicate the positions on the glass slide where AFM height images were recorded (see Figure 2i–vi). The corresponding surface pressure isotherm is shown in **Figure 3a** in terms of Π as a function of normalized trough area, A_{trough}/A_0. The AFM images reveal the hexagonal arrangement of the CS microgels with only some local defects, which do not affect the overall arrangement

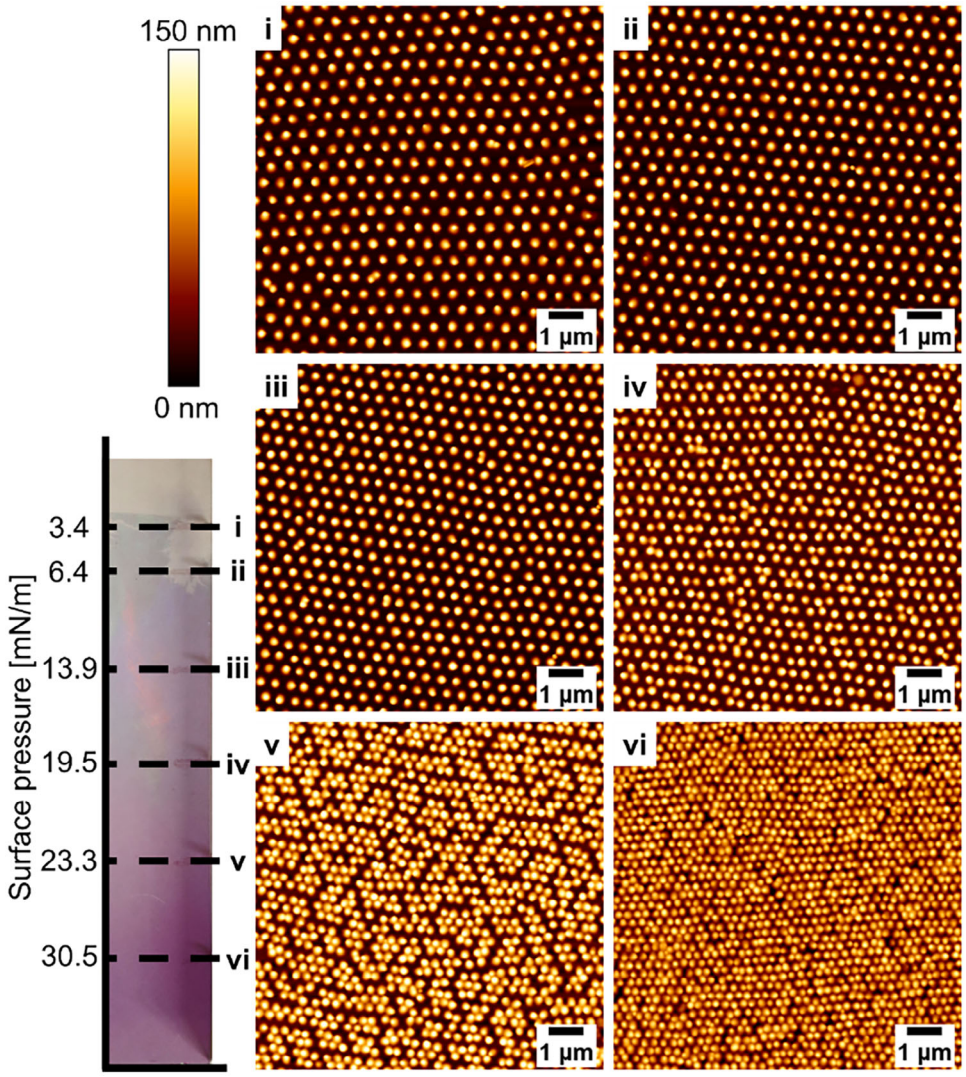

Figure 2. Ex situ analysis of the microgel monolayer after Langmuir-Blodgett deposition and subsequent drying. Bottom, left: Photograph of the glass substrate carrying the CS microgel monolayer. Horizontal, dashed lines mark surface pressure values and the corresponding positions where AFM analysis was performed. AFM height images of the monolayer corresponding to different surface pressures (i – vi). The z-scale bar (height) is shown on the top right and is the same for all presented AFM images.

at low compressions (images **i** to **iii**). These exemplary images show single crystalline domains over the entire scanned 100 µm^2 area. This underlines the very low size polydispersity of the CS microgels. Similar large domains were also previously reported for comparable CS microgels.[33,56] From image **i** to **iii** values of $d_{c\text{-}c}$ decrease from 502 ± 14 nm to 435 ± 2 nm, as determined from the radial distribution functions (RDF) that were calculated from the AFM height images. The fact that these distances are significantly larger than the value of D_h = 350 ± 3 nm measured from dilute dispersion in the swollen state (20 °C), is related to the lateral deformation (stretching) of the microgel shell to a diameter D_i at the interface as shown in Figure 1a–c. The ratio D_i/D_h depends on the shell-to-core size ratio, the shell softness as well as the overall dimensions.[25,65,66] We note that AFM images depict the monolayer in the dried state with significantly reduced microgel dimensions leading to the non-close-packed appearance. Upon further compression, we observe a further reduction in $d_{c\text{-}c}$ and the appearance of small clusters of microgels with significantly smaller spacings at 19.5 mN m^{-1}. The fraction of clusters of microgels in close proximity increases upon further compression. The clustering, observed in the AFM images **iv** to **vi**, is attributed to drying artefacts, that will be further discussed in the next sections. Despite these local changes, the overall microstructure still adopts hexagonal packing as confirmed by the fast Fourier transforms (FFTs) provided in Figure S4, Supporting Information. At 30.5 mN m^{-1}, we reach $d_{c\text{-}c}$ = 259 ± 3 nm, which is significantly smaller than D_h indicating that the microgel shells are in a compressed state. At higher surface pressures we approach the mechanical stability limit of the monolayer. We will later see that the region of monolayer failure can also be detected optically. **Table 1** summarizes the determined values of $d_{c\text{-}c}$ obtained from analysis of the AFM images performed at different values of Π along the surface pressure isotherm that will be discussed in the following.

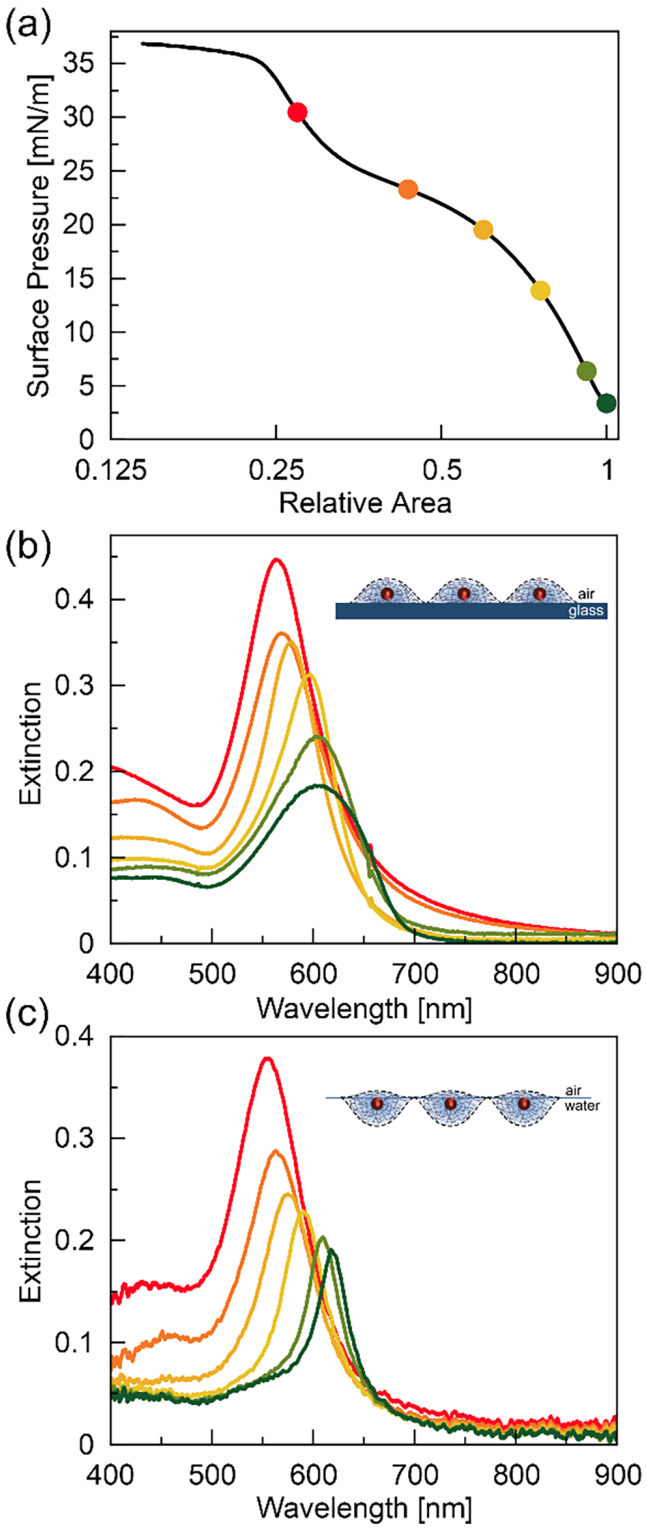

Figure 3. Optical response of assembled microgels with increasing surface pressure. a) Compression isotherm recorded at the air/water interface where the colored circles mark surface pressures at which extinction spectra are compared. b) Ex situ raw extinction spectra measured from the substrate-supported monolayer shown in Figure 2. c) In situ raw extinction spectra measured from the microgel monolayer at the air/water interface.

Table 1. Measured surface pressures, Π, and corresponding values of the nearest neighbor center-to-center distance, $d_{c\text{-}c}$, determined from the position of the first peak in RDFs computed from AFM height images.

Π [mN m^{-1}]	$d_{c\text{-}c}$ [nm]
3.4	502 ± 14
6.4	476 ± 7
13.9	435 ± 2
19.5	388 ± 1
23.3	286 ± 1
30.5	259 ± 3

4.2. Evolution of Plasmon Resonance Coupling: Qualitative Picture using In Situ Versus Ex Situ Spectroscopy

During the compression of the monolayer, we observe a color change from light pinkish with slight iridescence (Figure 1e,f) to intense pink (Figure 1g). To follow these changes spectroscopically, we first analyze the substrate-supported monolayer shown in Figure 2. The colored dots in Figure 3a mark surface pressures at which we will directly compare spectra recorded at the fluid interface (in situ) and upon transfer to the substrate (ex situ). We note that the AFM images provided in Figure 2 correspond to these selected values of Π. Figure 3b shows spectra for different degrees of compression recorded ex situ at the different positions on the substrate. The spectra reveal single resonance peaks that clearly change in response to the monolayer compression. At Π = 3.4 mN m^{-1} we observe a resonance peak with its peak position at λ_{max} = 605 nm and a peak width (full width at half maximum, FWHM) of FWHM = 150 nm. This peak is significantly redshifted compared to the peak measured from dilute, aqueous dispersion shown in Figure S5, Supporting Information (λ_{max} = 581 nm, FWHM = 133 nm). As reported by Ponomareva et al.,[33] this redshift is mostly caused by the change in the effective refractive index (RI) environment with water ($n \approx 1.33$) and highly water-swollen microgel shells in dispersion and the high RI glass as substrate ($n \approx 1.52$), air (n = 1.00) as superstrate and the collapsed microgel shell surrounding the AuNP cores in case of the substrate-supported monolayer. To decouple the influence of the RI environment from potential electromagnetic interactions in our periodic arrays, we also prepared a very dilute, random submonolayer on a glass substrate. The corresponding extinction spectrum in Figure S6, Supporting Information shows a resonance peak at λ_{max} = 594 nm with FWHM = 132 nm. While the peak width matches closely to the one measured from dilute dispersion, the redshift of the resonance by 13 nm underlines that the effective RI environment has a larger value as compared to the RI of water in the case of the measurement from dispersion. As visible in Figure 3b, with increasing Π, the resonance peak blueshifts, gains in intensity and the FWHM reduces. The increase in intensity is mostly related to the increase in number of particles per area, N_p, as the interparticle spacing is reduced upon compression.

To follow this change in situ, at the air/water interface, we combined a Langmuir trough with an optical fiber-based extinction spectrometer. With this setup, it is possible to measure the

surface pressure and extinction spectra simultaneously during the continuous compression of the monolayer. Since the continuous compression of the monolayer is expected to lead to a change in the lateral and vertical microgel morphology leading to an increase in polymer volume fraction in the interfacial film which might affect any scattering background, we first performed reference measurements. For these measurements we used the CS microgels with the initial small AuNP cores (D_{core} = 14 nm) prior to overgrowth. The optical response of these microgels in dispersion (Figure S5, Supporting Information) is dominated by the strong light scattering of the microgel shell and the cores contribute only with a small, purely absorptive resonance component.[18,67] Figure S7, Supporting Information shows spectra recorded during the uniaxial compression of the microgel monolayer. Independent of the state of compression measured extinctions are close to zero over the whole spectral range. This proves that: i) The extinction cross-section of the small AuNP cores is too low for in situ analysis of the plasmonic response of a monolayer, and ii) Scattering from the microgel shell is low, does not significantly contribute to the measured extinction and also does not change with monolayer compression. Therefore, we continue our experiment with the Au-PNIPAM microgels with overgrown cores (D_{core} = 96 nm) that show significantly enhanced plasmonic extinction. Figure 3c shows the spectra recorded in situ for the different points on the compression isotherm as highlighted in Figure 3a. Generally, we observe similar trends in the evolution of the peak position and intensity as found for the substrate-supported monolayer (ex situ). In contrast the FWHM in the range of small Π where values of $d_{c\text{-}c}$ are largest are significantly smaller for the monolayer at the fluid interface. At 3.4 mN m^{-1} (dark green), a narrow resonance peak at λ_{max} = 619 nm with FWHM = 50 nm is observed. Compared to the spectrum measured from dilute, aqueous dispersion shown in Figure S5, Supporting Information (λ_{max} = 581 nm, FWHM = 133 nm), the peak from the monolayer is significantly redshifted with a much smaller peak width pointing to constructive electromagnetic coupling.

4.3. Evolution of Plasmon Resonance Coupling: Quantitative Picture from In Situ Spectroscopy

In order to understand the spectral changes of the plasmonic monolayer at the air/water interface more quantitatively, we need to link the compression to changes in $d_{c\text{-}c}$. We do this by using the microstructural information obtained by AFM (ex situ) at 3.4 mN m^{-1} as a reference point. At this surface pressure, the microgels are highly ordered with no evidence of clustering as shown in Figure 2i. Thus, it is safe to assume that this microstructure also resembles the structure at the air/water interface. To estimate the total number of microgels (N_{total}) at the interface, we counted the number of particles from three different AFM images resulting in the number of microgels per area (*N/area*). By multiplying *N/area* by the total area of the trough (A_{trough}) at 3.4 mN m^{-1}, N_{total} can be derived. We then can calculate the available area per microgel ($A_{available}$) for each step of the compression experiment by dividing the respective trough area by N_{total}. Because of the hexagonal arrangement of the microgels we need to consider the maximum area fraction for 2D arrangement of spherical

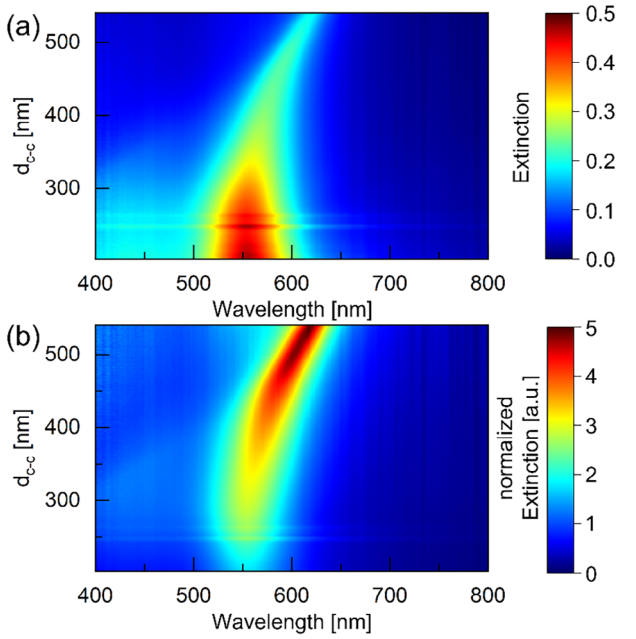

Figure 4. Spectral evolution of the resonance peak during continuous reduction in $d_{c\text{-}c}$ from in situ spectroscopy at the air/water interface. a) Extinction data as recorded. b) Normalized extinction spectra. Normalization was done by dividing each spectrum by the corresponding value of *N/area*.

objects of $\frac{\pi}{2\sqrt{3}} \approx 0.91$. Values of $d_{c\text{-}c}$ can then be calculated for the whole isotherm by:

$$d_{c-c} = \sqrt{\frac{A_{available} \cdot 0.91 \cdot 4}{\pi}} \quad (2)$$

We want to note that this calculation might underestimate real interparticle distances in the range of high compressions, where the microgels are significantly compressed which might lead to faceting and consequently area fractions >0.91. Due to the square root in equation 2 this effect however, is almost negligible.

Figure 4a shows the full series of extinction spectra (>1800) for decreasing $d_{c\text{-}c}$ from top to bottom. One clearly observes the continuous blueshift from large $d_{c\text{-}c}$, at the beginning of the compression experiment, down to ≈300 nm. For even smaller values of $d_{c\text{-}c}$ the resonance position remains almost constant. The blueshift is accompanied by a continuous broadening of the resonance peak. In the range of $d_{c\text{-}c}$ < 270 nm, jumps in intensity and peak width occur. These "jumps" are related to the failure of the monolayer in the regime of large compressions. Here, we assume the monolayer to buckle and break, ultimately leading to mass transport to the subphase. It is possible that at intermediate steps, domains from the colloidal monolayer stack on top of each other which would explain the jumps in intensity. While in this work our aim was to measure the full compression isotherm including the regime of monolayer failure, we want to note that at intermediate surface pressures we expect the monolayer to reversibly respond to increases/decreases in available trough area. This has been shown for similar CS microgels in a very recent

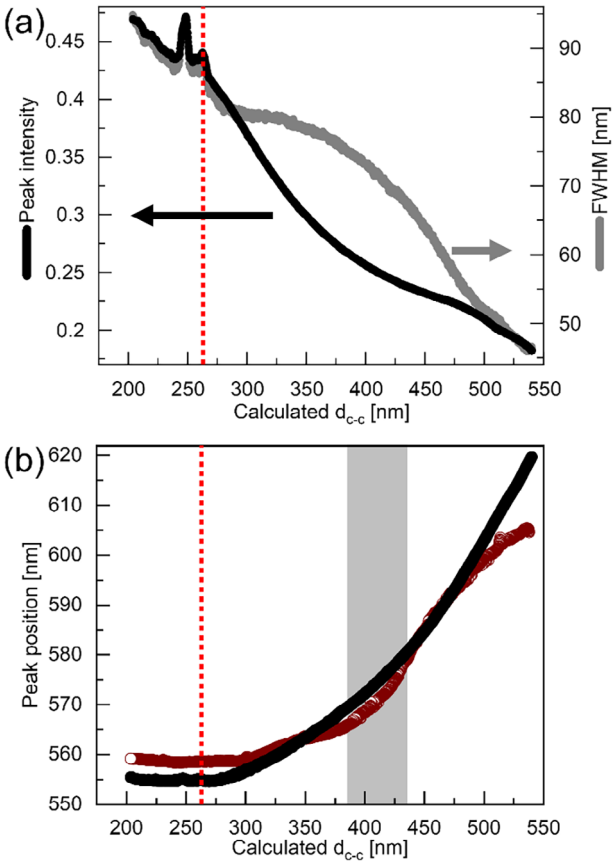

Figure 5. Results from automated peak fitting. a) Intensity (black symbols) and FWHM (grey symbols) of the resonance peak as a function of $d_{c\text{-}c}$. b) Peak position determined from in situ spectroscopy at the air/water interface (black circles) and from the substrate-supported monolayer (ex situ, open brown circles) as a function of $d_{c\text{-}c}$. The grey shaded area marks the regime of particle distances where the beginning of clustering was observed in case of the sample transferred to the substrate. The vertical red dashed lines in both diagrams indicate the critical interparticle distance for which mechanical failure of the monolayer was observed to begin.

work.[68] In that work we have shown that after multiple cycles, CS microgels always reached similar values of $d_{c\text{-}c}$ at the same surface pressures. Thus, for the present plasmonic system we would expect that the resonance shifts will also be reversible with respect to changes in the trough area. Since we know the number of particles per unit area for each spectrum, we can normalize the extinction spectra to eliminate the effect of the increasing number of microgels probed during the compression experiment. Figure 4b shows the normalized spectra as a function of $d_{c\text{-}c}$. Plotting the data this way it becomes clearer that we start with an intense and sharp resonance at large values of $d_{c\text{-}c}$ that broadens, loses intensity and shifts to smaller wavelengths as $d_{c\text{-}c}$ is decreased.

With the PeakAnalyzer script we analyzed the large number of spectra recorded in an automated fashion to extract the peak position, intensity and FWHM. **Figure 5a** shows the peak intensity (left axis, black) and FWHM (right axis, grey) from the in situ experiment as a function of $d_{c\text{-}c}$. The peak intensity (not normalized) increases continuously until jumps in intensity are observed in the regime of mechanical monolayer failure. The approximate $d_{c\text{-}c}$ where this begins is highlighted by the vertical, red dashed line. The evolution of the peak intensity outside the region of monolayer failure clearly does not follow the expectation for increasing number of optically non-interacting particles according to the Beer-Lambert law. This is also visible in Figure 4b where the maximum peak intensity does not remain constant albeit the normalization by the changing number of particles per area. The FWHM increases from initial values below 50 nm to values approaching ≈90 nm when the monolayer is compressed. These values are significantly lower than the ones measured from dilute, aqueous dispersion. The filled black circles in Figure 5b correspond to the peak positions that continuously blueshift with decreasing $d_{c\text{-}c}$ until the value remains constant in the regime of monolayer failure. The fact that the blueshift of the peak position is continuous indicates that also the change in interparticle distance is continuous. This means that from the in situ measured spectral changes there is no indication for clustering of microgels at the fluid interface, as was observed from the ex situ AFM analysis (images iv to vi in Figure 2). This is in agreement with our recent works, where we have shown that capillary interactions alter the microstructure of a microgel monolayer during drying on a substrate.[28,64] At large values of $d_{c\text{-}c}$ where we observed the intense and narrow resonance peak, the peak position depends almost linearly on $d_{c\text{-}c}$. The near linear correlation between resonance position and particle distance indicates that the mode has a pronounced photonic character due to constructive interference of the oscillating dipoles of the array. For a 2D periodic lattice, the interplanar spacing d is related to the lattice constant a by:[33]

$$\frac{1}{{d_{hk}}^2} = \frac{4}{3}\left(\frac{h^2 + hk + k^2}{a^2}\right) \tag{3}$$

Here h and k denote the Miller indices. For a hexagonal lattice, the nearest neighbor interparticle distance is the lattice constant, that is, $a = d_{c\text{-}c}$. Considering our largest estimated value of $d_{c\text{-}c}$ = 540 nm at the beginning of the compression experiment and using n_{eff} = 1.33 to account for water with a small fraction of polymer in the space in between the AuNPs in the thin colloidal film, we expect the primary photonic mode to occur at $\lambda_{10} = \frac{\sqrt{3}\, d_{c-c} \cdot n_{\text{eff}}}{2} \approx 618$ nm. At this wavelength we have a large spectral overlap with the uncoupled LSPR band (determined in aqueous solution, see Figure S5, Supporting Information). Indeed, our measured resonance mode at this $d_{c\text{-}c}$ is close to 618 nm. The significantly smaller line width of our resonance underlines that we deal with plasmonic surface lattice resonances (SLRs). Previous works have shown that a homogeneous refractive index (RI) environment is necessary to allow for coupling to in-plane modes of diffraction.[33,41–43] Although we deal with a low RI environment (mostly water surrounding the colloidal film) and an asymmetric RI environment due to the nearby air superstrate, collective coupling due to diffractive modes is still pronounced. This implies that the in-plane RI environment is rather homogeneous and sufficiently thick. In other words, the AuNPs are expected to be fully immersed in the water subphase as indicated in the sketch of Figure 1b. Since our excitation geometry (transmission) allows for dipole excitation that oscillate in-plane, out-of-plane penetration of the electromagnetic fields

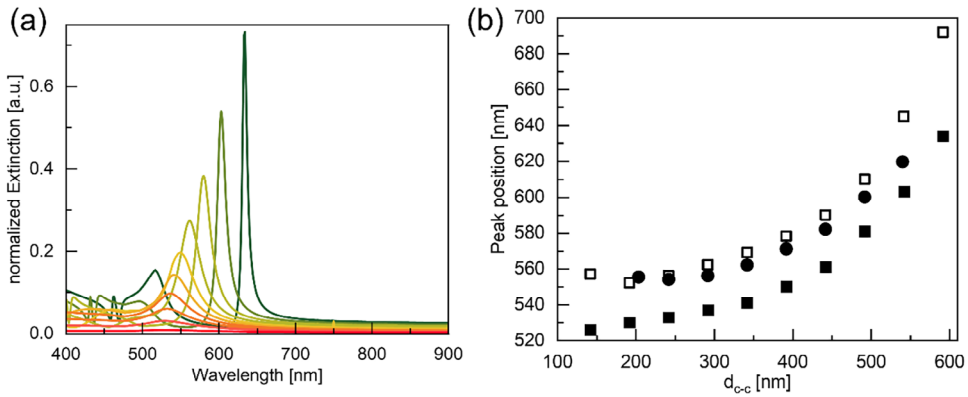

Figure 6. Comparison of the experiment with simulations. a) Simulated extinction spectra of assembled AuNPs at the air/water interface with $d_{c\text{-}c}$ from 142 to 592 nm in 50 nm steps. Spectra were normalized to the cross section per particle. The $d_{c\text{-}c}$ increases from dark red to dark green. b) Resonance peak positions plotted against $d_{c\text{-}c}$ from the experiment (filled circles), MLWA (open squares) and COMSOL (filled squares) simulations.

into the nearby air superstrate is expected to be low. We want to note that our coupling is relatively weak, leading to low quality factors due to the less-than-ideal RI conditions.[69] For similar self-assembled structures embedded in a homogeneous, higher RI environment Ponomareva et al. reported stronger plasmonic SLRs.[33] As $d_{c\text{-}c}$ decreases, the peak position shifts to shorter wavelengths and becomes broader, which is in good agreement with the findings of Ponomareva et al. At $d_{c\text{-}c} = 475$ nm the photonic mode should occur at $\lambda_{10} \approx 548$ nm for RI = 1.33. This means the diffraction edge is located on the high energy side of the (uncoupled) LSPR. Here the real part of the inverse of the AuNP polarizability ($1/\alpha$) and the dipole sum (S) have the same sign and conditions for coherent plasmonic-diffractive coupling are not met.[41] Further reduction in $d_{c\text{-}c}$ further blueshifts the resonance while the FWHM increases indicating weaker coupling and significant damping. While the resonance width for smallest distances is still below the width of the LSPR measured in dilute aqueous dispersion, it seems to approach the width of uncoupled (isolated) AuNPs. We want to note that we could not measure extinction spectra of a random CS microgel monolayer or even isolated CS microgels at the air/water interface to capture the uncoupled state in the relevant RI environment. At the highest surface pressure of 30.5 mN m^{-1}, the peak position is at $\lambda_{max} =$ 555 nm. We want to note that our values of $d_{c\text{-}c}$ in the experiments at the air/water interface are too large to support near-field coupling that would lead to a redshift of the resonance with decreasing interparticle distance with a coupling strength that scales with $1/{d_{c\text{-}c}}^3$.[70]

In Figure 5b we also plot peak positions determined from the substrate-supported monolayer (open, brown circles) that features an even stronger mismatch in RI environment as discussed previously. While we also observe a continuous blueshift with decreasing $d_{c\text{-}c}$ there are some pronounced differences to the positions determined in situ at the air/water interface. Unlike the case for particles at the air/water interface, at large $d_{c\text{-}c}$ values the peak position for the substrate-supported monolayer seems to be slowly asymptoting and does not follow the predicted linear trend. There is no indication for pronounced to in-plane diffractive modes. For a strongly asymmetric RI environment such plasmonic arrays are not expected to support plasmonic SLRs.[33,41] For $d_{c\text{-}c}$ values smaller than 480 nm, the data from both experiments overlap until $d_{c\text{-}c} \approx 435$ nm. The grey shaded area between $d_{c\text{-}c}$ of 435 to 388 nm marks the region where clustering of microgels was observed in the AFM images **iv** to **vi**. Analysis of these clusters revealed interparticle distances that decrease from ≈250 – 300 nm down to ≈200 nm at maximum compression. Thus, for the substrate supported sample we might enter regions where near-field coupling could potentially start to become relevant. The fact that the peak positions emerge less monotonically in this region and down to values of $d_{c\text{-}c}$ of 300 nm might imply that near-field coupling due to the growing fraction of clusters on the substrate is indeed relevant. Since we are in the regime of weak coupling with many potential influences on the coupling scenario of the substrate, we do not want to overinterpret our findings.

To support our findings from the extinction measurements at the air/water interface and in particular the coupling to diffractive modes in the range of large distances, we will now turn to results from analytical calculations.

4.4. Calculations using the Coupled Dipole Approximation

The coupled dipole approximation was used to model the optical properties of lithographically prepared particle arrays by Schatz et al.[71,72] and by Barnes et al.[43,73] Using the modified long wavelength approximation (MLWA), the polarizability of a spherical particle is given by

$$\alpha_{\mathrm{MLWA}} = \frac{\alpha_{\mathrm{dipole}}}{1 - \frac{2}{3} i k^3 \alpha_{\mathrm{dipole}} - \frac{k^2}{a} \alpha_{\mathrm{dipole}}} \tag{4}$$

Here the static polarizability of a small isolated sphere is given by

$$\alpha_{\mathrm{dipole}} = a^3 \, \frac{\epsilon - \epsilon_{\mathrm{m}}}{\epsilon + 2\epsilon_{\mathrm{m}}} \tag{5}$$

where a is the particle radius, $\epsilon_{\mathrm{m}} = 1.78$ is the dielectric constant of the non-absorbing solvent, and ϵ is the dielectric function of the metal NP. Equation 5 accounts for retardation and radiative damping in particles larger than the dipole limit. It is used to

model the experimental spectra of our AuNPs in water (see Supporting Information). When the particles are incorporated into a 2D hexagonal lattice, the local field is affected by the coherent superposition of the fields scattered by the other AuNPs in the lattice. The modified polarizability, α_{latt} can be written:

$$\alpha_{\text{latt}} = \frac{1}{\frac{1}{\alpha_{\text{MLWA}}} - S} \tag{6}$$

Here S is the sum of scattered electric fields due to all the other AuNPs in the neighborhood of the particle under consideration. It depends on the refractive index, the wavelength of the incident light and the lattice symmetry. The lattice sum S is complex valued and decays slowly. The modified absorption, scattering and extinction cross sections are given by:

$$C_{\text{abs}} = 4\pi k \ \text{Im}\left(\alpha_{\text{latt}}\right) \tag{7}$$

$$C_{\text{sca}} = \frac{8}{3}\pi k^4 \left|\alpha_{\text{latt}}\right|^2 \tag{8}$$

The total extinction coefficient is then found using

$$C_{\text{ext}} = C_{\text{abs}} + C_{\text{sca}} \tag{9}$$

4.5. Spectra of Isolated Particles

For AuNPs with radii of 46 nm, the extinction spectrum is due to both light scattering and absorption. In Figure S8, Supporting Information, we compare the experimental extinction spectrum from dilute aqueous dispersions of our CS microgels to calculated single particle spectra. The experimental LSPR peak wavelength is 581 nm. The peak is broadened primarily by polydispersity in the particle size. Also shown is the spectrum predicted using the MLWA model which yields a peak at 583 nm for a radius of 46 nm in excellent agreement with the experimental model. The good agreement also shows that the swollen PNIPAM shell in experiment has minor influence on the resonance position, that is, the RI is expected to be close to the value of water indicating a high water content in the shell. Spectra calculated using the full Mie theory, yields a surprisingly blue shifted peak at 560 nm (see Table S1, Supporting Information). Notably, the Mie curve does a much better job of matching the extinction at wavelengths shorter than the LSPR band. COMSOL modelling yields a peak at 584 nm for 46 nm gold spheres in water (not shown for clarity). Given the good fit to the MLWA model we can now calculate how such particles couple in an ordered 2D film.

4.6. Spectra of Hexagonal Arrays

In **Figure 6** we present the experimentally determined peak wavelengths for the CS microgel monolayer as a function of the separation together with the peak positions from coupled dipole approximation (MLWA model). In agreement with data from lithographically prepared particle arrays,[72] we find that the peak blueshifts with decreasing particle separation. At values of $d_{c\text{-}c}$ above about 600 nm, the shift is close to the expected shift for a purely photonic lattice mode where the peak is expected to shift according to equation 4. The slope of the curve should be linear with a value of $\frac{\lambda_{10}}{d_{c-c}} = \frac{\sqrt{3}n_{\text{eff}}}{2} \approx 1.15$. As the particle separation decreases, both the COMSOL and MLWA models show that the extinction cross-section per particle decreases and the FWHM increases dramatically. To understand the reasons for this, we note that resonances occur when the denominator in equation 7 approaches zero. In Figures S10 and S11, Supporting Information, we present two graphs highlighting the interplay between S and $1/\alpha$.

When the lattice constant is significantly larger than the LSPR wavelength (581 nm in water for 46 nm spherical gold particles), the SLR closely follows the prediction based on equation 4, where $\lambda_{10} = \frac{\sqrt{3}}{2} d_{c-c}\, n_{\text{eff}} \approx 682$ nm. A second resonance at ≈560 nm corresponds to the LSPR peak in water for the uncoupled AuNPs but it is not a pure LSPR. The MLWA model also predicts a weaker secondary peak at $\lambda_{11} = \frac{a}{2} n_{\text{eff}} \approx 393\ nm$. This peak was not resolved experimentally. These longer wavelength SLR peaks are orders of magnitude sharper and more intense than the LSPR peak. As the CS microgel monolayer is compressed particle extinction coefficient (per particle) decreases and the resonance blue-shifts as shown in Figure 3. Importantly, once the photonic mode merges with the interband transitions of the gold metal, at wavelengths < 510 nm, there is always a large value for both Re(α) and Im(α) and this weakens the coupling to in-plane diffractive modes.

In summary, the MLWA model accurately predicts the extinction peaks experimentally observed during the continuous compression of our CS microgel monolayer, as well as the decreasing intensities and broadening. At the smallest separations there is evidence for a small red-shift which reflects the onset of near-field coupling between the AuNPs.

4.7. COMSOL Calculations

Because the MLWA model is restricted to a homogeneous refractive index environment, it is worth exploring to what extent the asymmetric dielectric surroundings may influence the 2D films. Hence, the optical response of the AuNP monolayer at the air/water interface was investigated via finite element analysis (FEA) using COMSOL Multiphysics. Figure 6a shows simulated extinction spectra of the interfacial monolayers with $d_{c\text{-}c}$ values ranging from 592 to 142 nm, with 50 nm steps. These have been normalized to the cross section per particle. In agreement with the experiment, we observe a continuous broadening and blue shift of the resonance peak with decreasing $d_{c\text{-}c}$. For large $d_{c\text{-}c}$ values, the extinction peak is intense and narrow pointing to a more pronounced photonic character of the mode. As $d_{c\text{-}c}$ decreases, coupling to the diffractive mode weakens, leading to a reduction in peak intensity and an increase in FWHM due to damping.

Figure 6b shows a comparison of the peak positions determined from simulations and experiment. The data points from both simulations show the same trend as the experimental data. The absolute agreement however is significantly better for the calculations based on the coupled dipole approximation with the MLWA (open squares). Here the peak positions match the experimental values closely over the whole range of interparticle

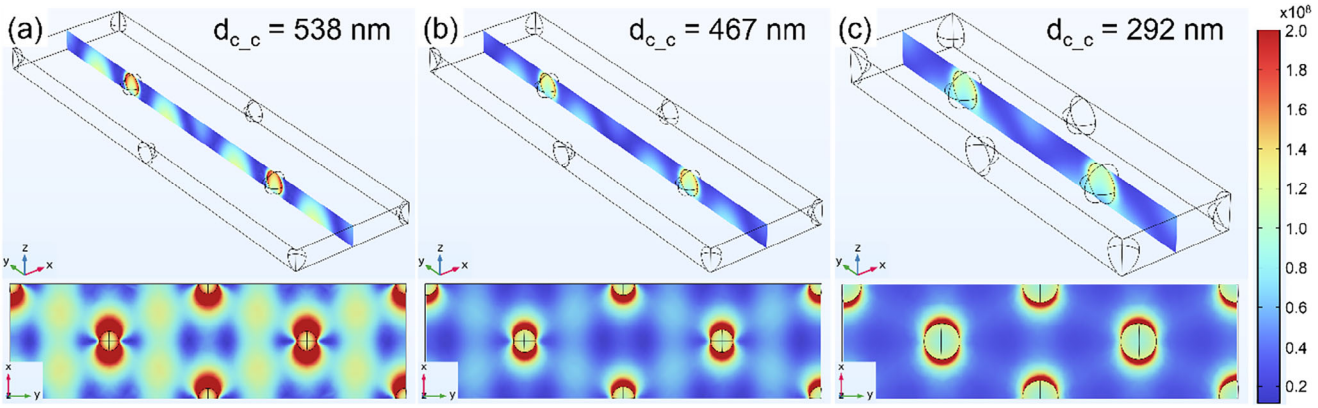

Figure 7. Calculated electromagnetic intensity maps for the hexagonally ordered monolayer a) at the beginning, b) at the middle, and c) at the end of the compression, respectively. The top and bottom row show two different angles of view. The same color scale applies to all maps.

distances. Slight deviations between experiment and simulation might be related to the more complex RI conditions in the experiments. The simulations assume a homogeneous medium with a fixed RI. However, in actual experiments, the microgel shells contribute to the effective RI in the interfacial layer and this contribution should also depend on the degree of compression. This is expected to slightly increase the RI compared to the value of a purely aqueous environment, and also to lead to local heterogeneities due to the "fried-egg"-like morphology of the stretched CS microgels at the air/water interface.

We then studied the optical response of the monolayer at different stages of compression. We decided on three different $d_{c\text{-}c}$ values: 538, 467, and 292 nm, which represent the start, the middle and the end of the compression process, respectively. The near-field electromagnetic intensity maps were simulated and constructed for the three cases and are shown in **Figure 7**. The intensities were calculated at the incident wavelength corresponding to their respective extinction peaks from the experiment. In all three maps, the excitation of the dipolar resonance can be clearly identified around the AuNPs. At the highest $d_{c\text{-}c}$, the high intensity between the particles can be ascribed to the in-plane diffractive band, which couples with the dipolar LSPR of the AuNPs. Thus, the narrow peak is ascribed to a plasmonic SLR as a result of the diffractive-plasmonic coupling. With decreasing $d_{c\text{-}c}$, the intensity of the diffractive band between the AuNPs decreases, leading to weakening of the plasmonic SLR. Thus, the peak becomes broader and shifts to lower wavelengths as the interparticle distance decreases. Importantly, we have shown that we can tune the relative intensities and coupling of the diffractive and plasmon modes in these 2D ordered lattices by tuning the interparticle spacing.

5. Conclusions

In this work, we have analyzed the optical response of plasmonic core-shell microgels at the air/water interface in situ under continuous compression in a Langmuir trough. The experimental setup allows measurement of the monolayer extinction in transmission geometry with a temporal resolution of seconds – very fast compared to the duration of the total compression experiment. Thereby we can follow changes in the optical response related to sub-nm changes in interparticle spacing. We have calculated the interparticle distance of the microgels at the interface by analyzing their microstructure ex situ at the maximum available area, that is, at low states of compression. Under these conditions monolayer transfer to solid substrates is not affected by capillary interactions which lead to microgel clustering. This has allowed us to correlate the $d_{c\text{-}c}$ of the microgels with the peak positions in the in situ extinction spectra. We observe a continuous blueshift and broadening of the resonance mode with decreasing interparticle distance. The observed spectral changes are related to coupling of the single particle plasmon resonances to in-plane diffractive modes. In the range of large distances this collective coupling leads to pronounced plasmonic surface lattice resonances with peak maxima that closely follow the main photonic mode. As the interparticle distance decreases the coupling strength weakens. This finding is supported by both MLWA calculations and COMSOL simulations. Most importantly the blueshift in resonance position as the interparticle distance decreases matches closely the experimental data.

This study demonstrates a relatively easy, fast and non-destructive approach to analyze plasmonic colloidal monolayers at the air/water interface upon reduction of the interparticle distance. Small changes in the optical response can be directly monitored and linked to the surface pressure providing a direct link to the interparticle distance. The setup not only facilitates on-demand tailoring of the microstructure of the monolayer, but also enables further studies of the microgel shell and its behavior at different surface pressure. The high sensitivity of the peak position offers immediate feedback on any change between the microgels. This will enable a better understanding of core-shell microgels, which are too small in size for light microscopy analysis. In future works, it might be interesting to study the regime of stronger coupling for example by using silver instead of gold nanoparticle cores and by using a liquid subphase with a higher refractive index.

Supporting Information

Supporting Information is available from the Wiley Online Library or from the author.

Acknowledgements

The authors acknowledge the German Research Foundation (DFG) and the state of NRW for funding the cryo-TEM (INST 208/749–1 FUGG) and Marius Otten from Heinrich Heine University Düsseldorf for his assistance with the operation and image recording. M.K. acknowledges the German Research Foundation (DFG) for funding under grant KA3880/6-1. D.F. acknowledges the Luxembourg National Research Fund (FNR), Project Reference 15688439. Open access funding enabled and organized by Projekt DEAL. P.M. and J.W. thank the ARC for support under Grant CE170100026.

Conflict of Interest

The authors declare no conflict of interest.

Author Contributions

M.K. and D.F. designed the study. D.F. synthesized the core-shell microgels and performed the characterization including dynamic light scattering and transmission electron microscopy. J.K. designed and 3D-printed the first version of the fiber holder. C.W. optimized the holder and conducted preliminary experiments with the self-built setup. D.F. prepared the monolayer via Langmuir-Blodgett deposition and characterized the monolayer by atomic force microscopy and extinction spectroscopy. Further processing of the images was performed by D.F. D.F. conducted and analyzed the in situ experiment and combined the results to the ex situ measurements. J.W. performed COMSOL simulations to support experimental findings and helped with the interpretation of the results. P.M. carried out the MLWA modelling. J.A.M. and J.M. provided the PeakAnalyzer script to extract different parameters, such as peak position from the extinction spectra. D.F. designed and prepared all the figures and wrote the first version of the manuscript. M.K. performed editing and all authors contributed with helpful discussions and proofread the manuscript.

Data Availability Statement

The data that support the findings of this study are available from the corresponding author upon reasonable request.

Keywords

core-shell microgels, fluid interface, in situ spectroscopy, plasmonic-diffractive coupling, self-assembly

Received: May 22, 2025
Revised: July 22, 2025
Published online: August 29, 2025

[1] Y. N. Xia, Y. J. Xiong, B. Lim, S. E. Skrabalak, *Angew. Chem., Int. Ed.* **2009**, *48*, 60.
[2] L. M. Liz-Marzán, *Langmuir* **2006**, *22*, 32.
[3] K. Van Gordon, R. Girod, F. Bevilacqua, S. Bals, L. M. Liz-Marzan, *Nano Lett.* **2025**, *25*, 2887.
[4] L. Qiao, Z. Fu, J. Li, J. Ghosen, M. Zeng, J. Stebbins, P. N. Prasad, M. T. Swihart, *ACS Nano* **2017**, *11*, 6370.
[5] K. Boldt, N. Kirkwood, G. A. Beane, P. Mulvaney, *Chem. Mater.* **2013**, *25*, 4731.
[6] C. L. Bassani, G. van Anders, U. Banin, D. Baranov, Q. Chen, M. Dijkstra, M. S. Dimitriyev, E. Efrati, J. Faraudo, O. L. Gang, N. Gaston, R. Golestanian, G. I. Guerrero-Garcia, M. Gruenwald, A. Haji-Akbari, M. Ibañez, M. Karg, T. Kraus, B. Lee, R. C. Van Lehn, R. J. Macfarlane, B. M. Mognetti, A. Nikoubashman, S. Osat, O. V. Prezhdo, G. M. Rotskoff, L. Saiz, A. C. Shi, S. Skrabalak, I. I. Smalyukh, et al., *ACS Nano* **2024**, *18*, 14791.
[7] M. Grzelczak, J. Vermant, E. M. Furst, L. M. Liz-Marzán, *ACS Nano* **2010**, *4*, 3591.
[8] M. A. Boles, M. Engel, D. V. Talapin, *Chem. Rev.* **2016**, *116*, 11220.
[9] S. J. Tan, M. J. Campolongo, D. Luo, W. L. Cheng, *Nat. Nanotechnol.* **2011**, *6*, 268.
[10] C. A. Mirkin, R. L. Letsinger, R. C. Mucic, J. J. Storhoff, *Nature* **1996**, *382*, 607.
[11] A. P. Alivisatos, K. P. Johnsson, X. G. Peng, T. E. Wilson, C. J. Loweth, M. P. Bruchez, P. G. Schultz, *Nature* **1996**, *382*, 609.
[12] S. Y. Park, A. K. R. Lytton-Jean, B. Lee, S. Weigand, G. C. Schatz, C. A. Mirkin, *Nature* **2008**, *451*, 553.
[13] D. Nykypanchuk, M. M. Maye, D. van der Lelie, O. Gang, *Nature* **2008**, *451*, 549.
[14] N. K. Beyeh, Nonappa, V. L., J. Mikkilä, A. Korpi, D. Bochicchio, G. M. Pavan, O. Ikkala, R. H. A. Ras, M. A. Kostiainen, *ACS Nano* **2018**, *12*, 8029.
[15] M. Girard, J. A. Millan, M. O. de la Cruz, *Annu. Rev. Mater. Res.* **2017**, *47*, 33.
[16] R. Contreras-Cáceres, A. Sánchez-Iglesias, M. Karg, I. Pastoriza-Santos, J. Pérez-Juste, J. Pacifico, T. Hellweg, A. Fernández-Barbero, L. M. Liz-Marzán, *Adv. Mater.* **2008**, *20*, 1666.
[17] S. L. Wu, M. N. Zhu, Q. Lian, D. D. Lu, B. Spencer, D. J. Adlam, J. A. Hoyland, K. Volk, M. Karg, B. R. Saunders, *Nanoscale* **2018**, *10*, 18565.
[18] M. Karg, S. Jaber, T. Hellweg, P. Mulvaney, *Langmuir* **2011**, *27*, 820.
[19] M. Karg, *Macromol. Chem. Phys.* **2016**, *217*, 242.
[20] M. Karg, T. A. F. König, M. Retsch, C. Stelling, P. M. Reichstein, T. Honold, M. Thelakkat, A. Fery, *Mater. Today* **2015**, *18*, 185.
[21] M. J. Bergman, N. Gnan, M. Obiols-Rabasa, J. M. Meijer, L. Rovigatti, E. Zaccarelli, P. Schurtenberger, *Nat. Commun.* **2018**, *9*, 5039.
[22] P. S. Mohanty, D. Paloli, J. J. Crassous, E. Zaccarelli, P. Schurtenberger, *J. Chem. Phys.* **2014**, *140*, 094901.
[23] D. Paloli, P. S. Mohanty, J. J. Crassous, E. Zaccarelli, P. Schurtenberger, *Soft Matter* **2013**, *9*, 3000.
[24] A. Rauh, N. Carl, R. Schweins, M. Karg, *Langmuir* **2018**, *34*, 854.
[25] A. Rauh, M. Rey, L. Barbera, M. Zanini, M. Karg, L. Isa, *Soft Matter* **2017**, *13*, 158.
[26] M. Hildebrandt, D. P. Thuy, J. Kippenberger, T. L. Wigger, J. E. Houston, A. Scotti, M. Karg, *Soft Matter* **2023**, *19*, 7122.
[27] M. Rey, A. D. Law, D. M. A. Buzza, N. Vogel, *J. Am. Chem. Soc.* **2017**, *139*, 17464.
[28] K. Kuk, V. Abgarjan, L. Gregel, Y. Zhou, V. Carrasco Fadanelli, I. Buttinoni, M. Karg, *Soft Matter* **2023**, *19*, 175.
[29] H. Robertson, J. Zimmer, A. S. Name, C. Lux, S. Stock, R. von Klitzing, O. Soltwedel, *arXiv* **2025**, https://doi.org/10.48550/arXiv.2503.14181.
[30] A. Rubio-Andrés, D. Bastos-González, M. A. Fernandez-Rodriguez, *J. Colloid Interface Sci.* **2025**, *688*, 328.
[31] Y. C. Zhou, J. J. Crassous, M. Karg, *Langmuir* **2025**, *41*, 9274.
[32] M. Rey, M. A. Fernández-Rodríguez, M. Steinacher, L. Scheidegger, K. Geisel, W. Richtering, T. M. Squires, L. Isa, *Soft Matter* **2016**, *12*, 3545.
[33] E. Ponomareva, K. Volk, P. Mulvaney, M. Karg, *Langmuir* **2020**, *36*, 13601.
[34] K. Volk, J. P. S. Fitzgerald, M. Retsch, M. Karg, *Adv. Mater.* **2015**, *27*, 7332.
[35] T. Honold, K. Volk, A. Rauh, J. P. S. Fitzgerald, M. Karg, *J. Mater. Chem. C* **2015**, *3*, 11449.
[36] N. Vogel, C. Fernández-López, J. Pérez-Juste, L. M. Liz-Marzán, K. Landfester, C. K. Weiss, *Langmuir* **2012**, *28*, 8985.

[37] J. P. S. Fitzgerald, M. Karg, *Phys. Status Solidi A* **2017**, *214*, 1600947.
[38] A. M. Funston, C. Novo, T. J. Davis, P. Mulvaney, *Nano Lett.* **2009**, *9*, 1651.
[39] P. K. Jain, W. Y. Huang, M. A. El-Sayed, *Nano Lett.* **2007**, *7*, 2080.
[40] C. Cherqui, M. R. Bourgeois, D. Q. Wang, G. C. Schatz, *Acc. Chem. Res.* **2019**, *52*, 2548.
[41] V. G. Kravets, A. V. Kabashin, W. L. Barnes, A. N. Grigorenko, *Chem. Rev.* **2018**, *118*, 5912.
[42] V. G. Kravets, F. Schedin, A. N. Grigorenko, *Phys. Rev. Lett.* **2008**, *101*, 087403.
[43] B. Auguié, W. L. Barnes, *Phys. Rev. Lett.* **2008**, *101*, 143902.
[44] L. Zundel, J. R. Deop-Ruano, R. Martinez-Herrero, A. Manjavacas, *ACS Omega* **2022**, *7*, 31431.
[45] L. Zundel, A. May, A. Manjavacas, *ACS Photonics* **2021**, *8*, 360.
[46] V. Gupta, P. T. Probst, F. R. Gossler, A. M. Steiner, J. Schubert, Y. Brasse, T. A. F. König, A. Fery, *ACS Appl. Mater. Interfaces* **2019**, *11*, 28189.
[47] Y. Brasse, V. Gupta, H. C. T. Schollbach, M. Karg, T. A. F. König, A. Fery, *Adv. Mater. Interfaces* **2020**, *7*, 1901678.
[48] U. Cataldi, R. Caputo, Y. Kurylyak, G. Klein, M. Chekini, C. Umeton, T. Bürgi, *J. Mater. Chem. C* **2014**, *2*, 7927.
[49] J. Turkevich, P. C. Stevenson, J. Hillier, *Discuss. Faraday Soc.* **1951**, *11*, 55.
[50] A. Rauh, T. Honold, M. Karg, *Colloid Polym. Sci.* **2016**, *294*, 37.
[51] W. Kern, D. A. Puotinen, *Rca Rev.* **1970**, *31*, 187.
[52] C. A. Schneider, W. S. Rasband, K. W. Eliceiri, *Nat. Methods* **2012**, *9*, 671.
[53] S. Babar, J. H. Weaver, *Appl. Opt.* **2015**, *54*, 477.
[54] S. A. Vasudevan, A. Rauh, M. Kröger, M. Karg, L. Isa, *Langmuir* **2018**, *34*, 15370.
[55] J. S. J. Tang, R. S. Bader, E. S. A. Goerlitzer, J. F. Wendisch, G. R. Bourret, M. Rey, N. Vogel, *ACS Omega* **2018**, *3*, 12089.
[56] D. Feller, M. Otten, M. S. Dimitriyev, M. Karg, *Colloid Polym. Sci.* **2024**, *302*, https://doi.org/10.1007/s00396-024-05285-4.
[57] M. Rey, X. A. Hou, J. S. J. Tang, N. Vogel, *Soft Matter* **2017**, *13*, 8717.
[58] C. R. Harris, K. J. Millman, S. J. van der Walt, R. Gommers, P. Virtanen, D. Cournapeau, E. Wieser, J. Taylor, S. Berg, N. J. Smith, R. Kern, M. Picus, S. Hoyer, M. H. van Kerkwijk, M. Brett, A. Haldane, J. F. del Río, M. Wiebe, P. Peterson, P. Gérard-Marchant, K. Sheppard, T. Reddy, W. Weckesser, H. Abbasi, C. Gohlke, T. E. Oliphant, *Nature* **2020**, *585*, 357.
[59] J. Reback, W. McKinney, Pandas: powerful Python data analysis toolkit, https://doi.org/10.5281/zenodo.13819579.
[60] J. D. Hunter, *Comput. Sci. Eng.* **2007**, *9*, 90.
[61] P. Virtanen, R. Gommers, T. E. Oliphant, M. Haberland, T. Reddy, D. Cournapeau, E. Burovski, P. Peterson, W. Weckesser, J. Bright, S. J. van der Walt, M. Brett, J. Wilson, K. J. Millman, N. Mayorov, A. R. J. Nelson, E. Jones, R. Kern, E. Larson, C. J. Carey, I. Polat, Y. Feng, E. W. Moore, J. VanderPlas, D. Laxalde, J. Perktold, R. Cimrman, I. Henriksen, E. A. Quintero, C. R. Harris, et al., *Nat. Methods* **2020**, *17*, 352.
[62] Y. Gerelli, F. Camerin, S. Bochenek, M. M. Schmidt, A. Maestro, W. Richtering, E. Zaccarelli, A. Scotti, *Soft Matter* **2024**, *20*, 3653.
[63] L. H. Alvarez, A. A. Rudov, R. A. Gumerov, P. Lenssen, U. Simon, I. I. Potemkin, D. Wöll, *Phys. Chem. Chem. Phys.* **2021**, *23*, 4927.
[64] K. Kuk, J. Ringling, K. Graeff, S. Haensch, V. Carrasco-Fadanelli, A. A. Rudov, I. I. Potemkin, R. von Klitzing, I. Buttinoni, M. Karg, *Adv. Sci.* **2024**, *11*, 2406977.
[65] M. Destribats, V. Lapeyre, M. Wolfs, E. Sellier, F. Leal-Calderon, V. Ravaine, V. Schmitt, *Soft Matter* **2011**, *7*, 7689.
[66] K. Geisel, L. Isa, W. Richtering, *Langmuir* **2012**, *28*, 15770.
[67] E. Ponomareva, B. Tadgell, M. Hildebrandt, M. Krüsmann, S. Prévost, P. Mulvaney, M. Karg, *Soft Matter* **2022**, *18*, 807.
[68] V. Abgarjan, K. Kuk, J. L. S. Garthe, T. L. Wigger, M. Karg, *Soft Matter* **2025**, *21*, 5030.
[69] B. D. Thackray, V. G. Kravets, F. Schedin, G. Anton, P. A. Thomas, A. N. Grigorenko, *ACS Photonics* **2014**, *1*, 1116.
[70] D. Weber, P. Albella, P. Alonso-González, F. Neubrech, H. Gui, T. Nagao, R. Hillenbrand, J. Aizpurua, A. Pucci, *Opt. Express* **2011**, *19*, 15047.
[71] S. Zou, G. C. Schatz, *J. Chem. Phys.* **2005**, *122*, 097102.
[72] S. L. Zou, N. Janel, G. C. Schatz, *J. Chem. Phys.* **2004**, *120*, 10871.
[73] A. D. Humphrey, W. L. Barnes, *Phys. Rev. B* **2014**, *90*, 075404.